

In operando XAS study of atomic environment upon charge rate dynamic on the constant current stage in the graphene-coated Li-rich Mn-based cathode

Taehoon Kim^{a, *, 1}, Bohang Song^a, Alexander J.G. Lunt^a, Giannantonio Cibir^b, Andy Dent^b, Lu Li^c and Alexander M. Korsunsky^a

Abstract: Li₂O extraction from the electrode material is known to be the dominant mechanism of the irreversible battery capacity loss in the first cycle. The extraction mechanism of the Li⁺ ions shows dependence on the charge rate. Here for the first time we report the difference in the electrochemical behavior at two different charge rates (0.125 C vs 0.5 C) observed using novel design cells in the graphene-coated Li(Li_{0.2}Mn_{0.54}Ni_{0.13}Co_{0.13})O₂ cathode by *in operando* XAS. The results obtained from Mn, Co, and Ni XANES/EXAFS demonstrate that, whilst during fast charge Li₂O extraction is localized to the lithium slab in the crystal structure, the deintercalation is deeper at the slower charge rate, when Li⁺ ions are removed from both the transition metal and lithium layers. In the slow charge cell, Ni-O bond splittings resulting from Jahn-Teller distortion were clearly identified at approximately 4.224 V where a sudden rise in the bond length was observed in the Mn-O and Co-O EXAFS. The extraction from both layers exerts a significant effect on the crystal structure, as is evident from the two-phase reaction clearly identified in the slow charge cell. The results demonstrate the feasibility of novel cell design for *in operando* XAS.

Keywords: Lithium-ion batteries; Li-rich Mn based cathode; Graphene coating; Operando XAS

^aDepartment of Engineering Science, University of Oxford, Parks Road, Oxford, OX1 3PJ, UK.

^bBeamline B18, Diamond Light Source, Harwell Science & Innovation Campus, Didcot, Oxfordshire, OX11 0DE, UK.

^cDepartment of Mechanical Engineering, National University of Singapore, 9 Engineering Drive 1, Singapore 117576.

* Corresponding author, Department of Engineering Science, University of Oxford, Parks Road, Oxford, OX1 3PJ, UK.

¹ Qi Unit, Energy Materials and Surface Science, Okinawa Institute of Science and Technology (OIST), 1919-1 Tancha, Onna-son, Okinawa, 904-0495, Japan. E-mail: taehoon.kim@oist.jp

1. Introduction

Much interest has been aroused in the lithium-rich Mn-based composites as active materials for high capacity lithium-ion batteries. These systems described by the chemical formula $x\text{Li}_2\text{MnO}_3 \cdot (1-x)\text{LiMO}_2$ ($M = \text{Mn, Co, Ni}$) continue to have immense appeal as portable energy sources ranging from mobile devices to electric vehicles. The cathode of the active material benefits from high theoretical reversible capacity (over 250 mAhg^{-1}), good structural/thermal stability, high discharge capacity, and lower cost [1–8]. The lithium-rich Mn-based cathode that contains different transition metals, e.g. $\text{Li}(\text{Li}_{0.2}\text{Mn}_{0.54}\text{Ni}_{0.13}\text{Co}_{0.13})\text{O}_2$ offers advantages over compositions containing a single transition metal [9–14]. Both economical and ecological considerations lead to the use of transition metal composites as cathode materials. A major factor limiting the performance of the lithium-rich Mn-based cathode is the large irreversible capacity loss of 40-100 mAhg^{-1} during the first electrochemical cycle [15–19]. Li^+ ion extraction accompanied by oxygen release is known to be the dominant mechanism of the irreversible capacity loss [16,20–24]. A key factor for delivering high charge capacity in the lithium-rich systems is the structural integration of the two distinct crystallographic phases found in these systems, Li_2MnO_3 (monoclinic, $C2/m$) and LiMO_2 (trigonal, $R\bar{3}m$), where M denotes a transition metal ion (Mn, Ni or Co). At the crystal level, the structure of the composite can be visualised by the interleaving of close-packed layers from the two compounds, namely, the (001) planes from Li_2MnO_3 and the (003) planes from LiMO_2 with the interlayer spacing of $\sim 4.7 \text{ \AA}$, which allows the intimate integration of the two crystallographic components at the atomic level [3,25]. At the electrochemical level, this mixed metal oxide cathode material exhibits the two-phase reaction plateau around 4.4 V in the galvanostatic profile during initial charge.

The $x\text{Li}_2\text{MnO}_3 \cdot (1-x)\text{LiMO}_2$ cathode is composed of two main layers, namely, lithium-ion layer at 3a sites and transition metal layer at 3b sites that comprise a trigonal structure as illustrated in Fig. 1.

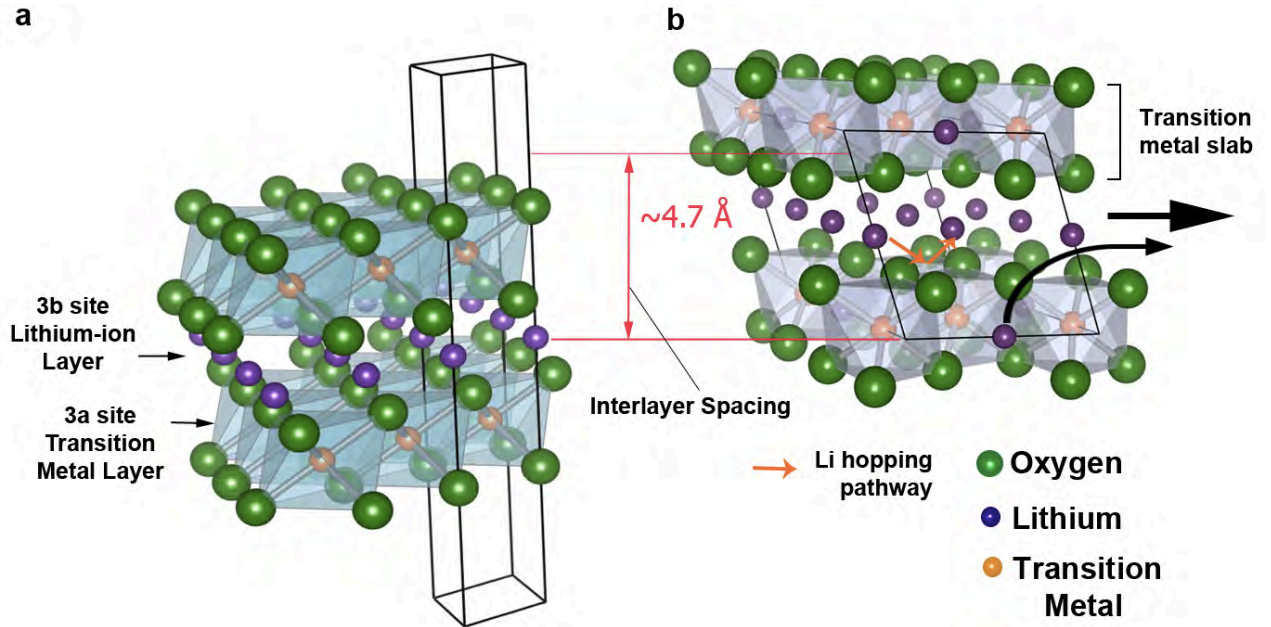


Fig. 1. Crystal structure of (a) LiMO_2 (trigonal, $R\bar{3}m$) and (b) Li_2MnO_3 (monoclinic, $C2/m$). Due to the presence of the interlayer spacing ($\sim 4.7 \text{ \AA}$), the crystal structure can be combined in an integrated composite. Black arrows indicates the extraction of the lithium-ions. In principle, Li^+ must be deintercalated from lithium layer and TM-layer either continuously or simultaneously during charge.

Li^+ not only occupies the lithium-layer in the $R\bar{3}m$, it can also partially occupy the transition metal layer in the $C2/m$ structure [22,23,25]. The lithium-ion surrounded by Mn^{4+} in the transition metal layer of $C2/m$ produces cation ordering which forms the Li_2MnO_3 structure [22,23,25]. It has been also proposed that the Li_2MnO_3 phase directly affects the electrochemical property and stability of the cathode [23,25,26]. Therefore, on the one hand Li_2MnO_3 contributes to the battery performance, but is also the main factor that leads to the capacity fading during electrochemical cycling. The removal of oxygen vacancies from the crystal lattice during the first charge reduces the number of available sites for Li^+ (de)intercalation [16,24,25]. This process is followed by the migration of the transition metals from the surface into the bulk of the active material [16,21,27]. It is likely that both the

removal of oxygen vacancies and the migration of transition metal ions during the first charge lead to the irreversible capacity loss in the lithium-ion batteries of this type.

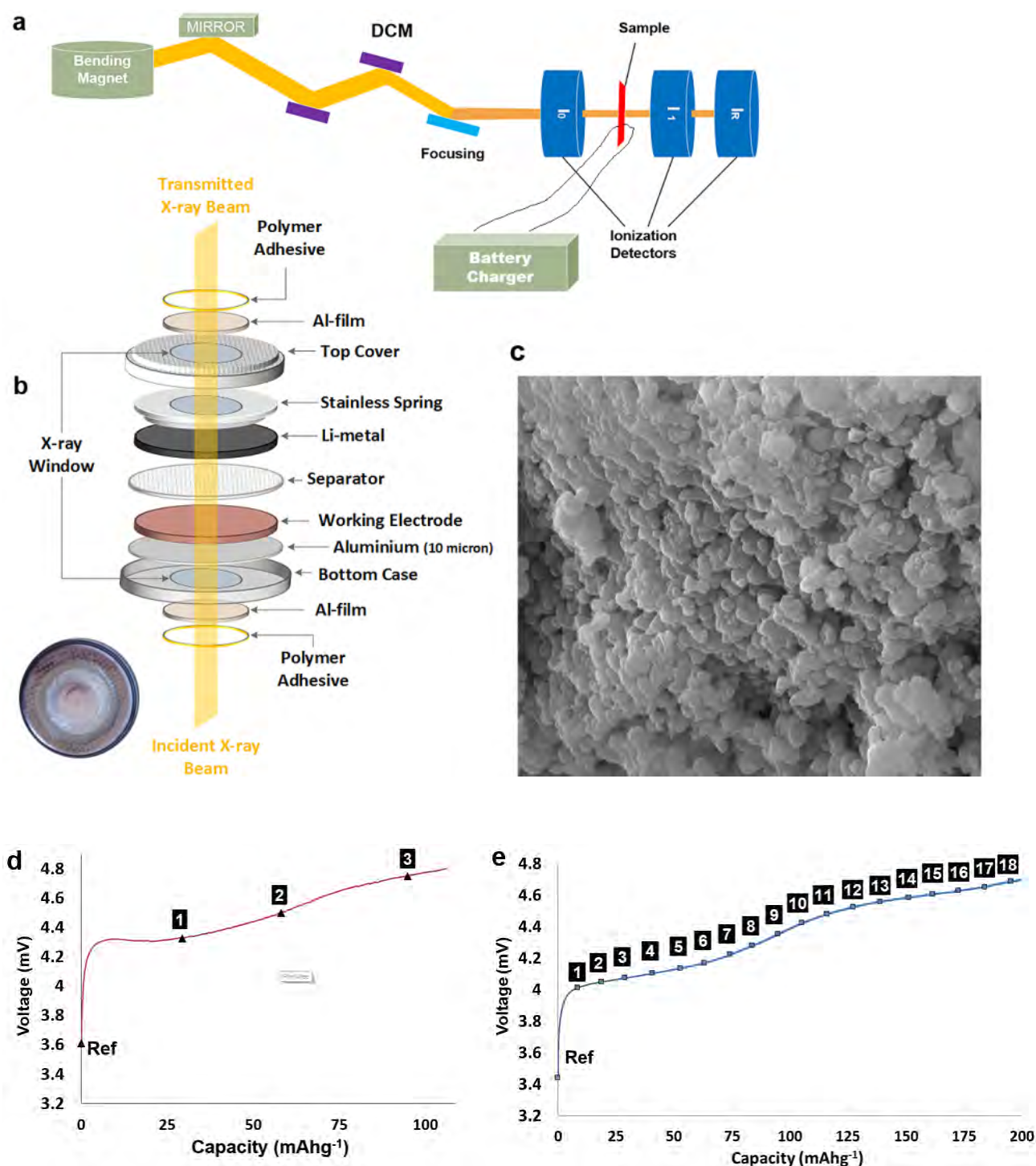


Fig. 2. In operando synchrotron investigation of lithium-ion batteries. (a) In Operando XAS setup. (b) Illustration of the special modified cell design. (c) Scanning Electron Microscopy of $\text{Li}(\text{Li}_{0.2}\text{Mn}_{0.54}\text{Ni}_{0.13}\text{Co}_{0.13})\text{O}_2$ cathode. (d) Galvanostatic profile of the operando cells at fast charge (0.5 C) and (e) slow charge (0.125 C) rates. Points signify the collection of XAS spectra numbered 1, 2 ...18, collected at charge points in the galvanostatic profile. Ref indicates the measurement of coin cell without any current.

In lithium-rich layered oxides, Li^+ ion mobility has become a central issue that needs to be elucidated to understand the performance and to improve the stability of the cathode. The cathode is composed of alternating layers, such as in the layered O3 structure, with the active material providing conduction pathways for the lithium-ions. The mechanism of lithium mobility in the crystal structure is usually explained by the Li^+ hopping mechanism between octahedral sites *via* an intermediate tetrahedral site [28,29]. An *ab initio* modelling study by Kang and Cedar suggests [28,29] that the Li slab spacing and the electrostatic repulsion between Li^+ and transition metals (Mn, Co, and Ni) determine the Li^+ mobility in the layered oxide structure. In this computation model, the activation barrier for the Li^+ diffusion decreases with the Li slab spacing. Li^+ mobility is highly sensitive to the distance between the oxygen layers (**Fig. 1**). The electrostatic repulsion between Li^+ and the transition metal ions at the tetrahedral sites is another major factor that affects the Li^+ mobility in the crystal structure [28]. Importantly, it is not only the presence of the transition metals at tetrahedral sites, but also their oxidation states that affect the mobility. Lower oxidation states result in weaker electrostatic interaction with the diffusing Li^+ ion [28]. It has been also suggested that the cation mixing influences the Li^+ mobility, and thus the battery performance [30,31]. It is therefore likely that the atomic-local environment surrounding Li^+ is strongly connected with the Li^+ mobility that is the key of the battery performance. The combined impacts from the inter-atomic reactions would be reflected in the galvanostatic profile.

To understand the irreversible capacity fading in the lithium-layered oxide, previous studies have been aimed at investigating the phase transitions of the cathode material during charge-discharge using *in situ* measurements such as *in situ* X-ray diffraction (XRD) [21,22,32–35], Raman spectroscopy [36–39], Nuclear Magnetic Resonance (NMR) spectroscopy [40] and X-ray absorption spectroscopy (XAS) [32,34,41–43].

In this study, we report *in operando* X-ray absorption spectroscopy (XAS) of graphene-coated $\text{Li}(\text{Li}_{0.2}\text{Mn}_{0.54}\text{Ni}_{0.13}\text{Co}_{0.13})\text{O}_2$ cathode coin cells of commercially available design with

specially created X-ray transmission window (**Fig. 2**). The cells have been successfully modified and thus can be used to examine the precise atomic environment of the host structure, as well as the inter-atomic reactions between transition elements during the first charge. The differences in the atomic environments resulting from the difference in the charge rates (0.125C vs 0.5C) in the “Li-rich layered” cathode are revealed here for the first time. It should be noted that the charge process was based on the constant current charge state. Although faster charge can be reached quicker at the target voltage, it doesn’t assure the full charge state. As such, a faster charge rate is likely to result in a lower capacity than that of the slow charge rate which is regarded as a deep charge. With this consideration, structural changes were quantified with the help of the Extended X-Ray Absorption Fine Structure (EXAFS). The Li^+ hopping mechanism is found to depend on the charge rate. Under higher applied current, Li^+ may (de)intercalate directly from one octahedral site to the next, as suggested by the evidence for this obtained from X-ray Absorption Near Edge Structure (XANES) and EXAFS. Furthermore, the two-phase reaction was clearly identified in the slow charge cell by EXAFS analyses, and the separation of the two local environments was observed at approximately 4.224 V for each transition metal. Whilst in the fast charging regime Li^+ is mostly extracted from the lithium-layer, in the slow charge it appears that Li^+ ions are extracted both from the transition metal layer and lithium-layer, which can be regarded as a deep charge process.

2. Experimental

The synthesis of the active material of $\text{Li}(\text{Li}_{0.2}\text{Mn}_{0.54}\text{Ni}_{0.13}\text{Co}_{0.13})\text{O}_2$ was done according to the spray-dryer assisted sol-gel method. Metal acetates of Mn, Ni, and Co (molar ratio Mn: Ni: Co = 0.54:0.13:0.13) were dissolved in a 200 mL aqueous solution (0.3 M). The dissolved solution was slowly dripped into a solution of 3% excess amount of lithium acetate and citric acid as a chelating agent with the identical stoichiometry as the metal ions, with continuous

stirring. This solution was dried by a spray-dryer (YC-015, Shanghai Politech Instrument & Equipment Co. Ltd) and further drying was carried out on the as-sprayed precursor at 80 °C overnight. Drying process was followed by the calcination at 800 °C for 15 h at a heating rate of 5 °C min⁻¹. The powders were cooled down in air after the calcination. The graphene coating was performed by a previous reported method [44]. Pristine material (0.3 g) was taken into 30 mL polyallylamine hydrochloride (PAH) with continuous stirring for 1 hr. Then, the pristine powders were added in the 15 ml graphene oxide aqueous solution (2 g/L) with continuous stirring for another 5 hr. This process was followed by the centrifugation, and the precipitated particles were washed three times. Those particles were added into L-ascorbic acid (LAA) aqueous solution at 95 °C for 30 min with continuous stirring. The synthesized powder was dried at 80 °C overnight. Finally, the coated powder was heat treated at 250 °C or 350 °C for 2h.

Specially-designed coin cells (CR-2025) with X-ray windows were used to conduct the *in operando* test. The electrode slurry was prepared by mixing the graphene-coated $\text{Li}(\text{Li}_{0.2}\text{Mn}_{0.54}\text{Ni}_{0.13}\text{Co}_{0.13})\text{O}_2$ (labelled as G-type), carbon black and polyvinylidene fluoride (PVDF) with the weight ratio of 80 : 10 : 10, respectively, in the n-methyl-2-pyrrolidone (NMP) solution. Then, it was constantly stirred for overnight to obtain homogenous dispersion. The prepared slurry was pasted onto an aluminium foil which was dried at 120 °C for overnight, prior to the cutting into many pieces of working electrodes with 12 mm diameter. As a half cell, the coin cells were assembled with the working electrodes (cathode), Li-foil (anode) and two pieces of separator (Celgard 2500). For the electrolyte, 1 M LiPF_6 in EC: DEC=1:1 organic solution was used. The diameter and thickness of the coin cells were 20 mm and 2.5 mm, respectively.

Synchrotron XAS was chosen for the *in operando* study. Beam experiment was performed on B18 Core EXAFS beamline at Diamond Light Source (DLS, UK). The size of the beam spot on the cells was approximately 140 x 140 microns. XAS spectra were collected in

transmission mode at the Mn (6.537 keV), Co (7.712 keV), and Ni (8.339 keV) K-edges using a Si (111) double crystal monochromator at room temperature. The beam energy was initially calibrated using Mn, Ni, and Co foils. The energy was tuned to 7.1 keV, 8.225 keV, and 9.3 keV, for Mn, Co, and Ni analysis respectively. The G1 (active material: 6.34 mg) cell was charged at a rate of 0.5C (0.634 mA), while the G2 cell (active material: 6.58 mg) was charged at a rate of 0.125C (0.164 mA) in the voltage window of 4.8-2.0 V vs. Li^0/Li^+ in which the 1C signifies 250 mA/g current density. The prepared coin cells were directly clamped to the galvanostatic charger (NEWARE Battery Test Station) with wires in order to perform the *in operando* XAS investigation.

Data interpretation was performed with ATHENA/ARTEMIS software package [45] using IFEFFIT code, by extracting the spectra data from EXAFS and XANES. The XAS data were normalized with a spline function, and the normalized EXAFS spectra were converted from energy (eV) to k-space and weighted by k^3 . This was followed by the Fourier transformation into R-space (uncorrected phase shift). Structural parameters such as the distance between the neighbouring shells, EXAFS Debye–Waller factor ($\exp(-2\sigma^2k^2)$), and the EXAFS R-factor were obtained by fitting within the ARTEMIS application with the FEFF 6 algorithm with atomic coordination number (CN) of 6 for Mn and Co. Multiple numbers of atomic coordination (e.g. CN=6, CN=4/2, CN=2/4) was chosen for the Ni EXAFS fitting during the first charge. The shift from the edge energy (ΔE_0) was also refined within the application. EXAFS fitting was carried out with two-phase system and the fitting ranges of the R-space were 0.98-3.75 Å, 1-3.8 Å, and 0.96-3.85 Å for Mn, Co, and Ni respectively.

3. Results

3.1. *In Operando* XANES at Mn K-edge

Using the novel design modified coin cells, high quality XANES spectra were collected at the K-edge in transmission mode. The distinctive difference in the charge dynamic is reflected in the Mn K-edge data presented in **Fig. 3**.

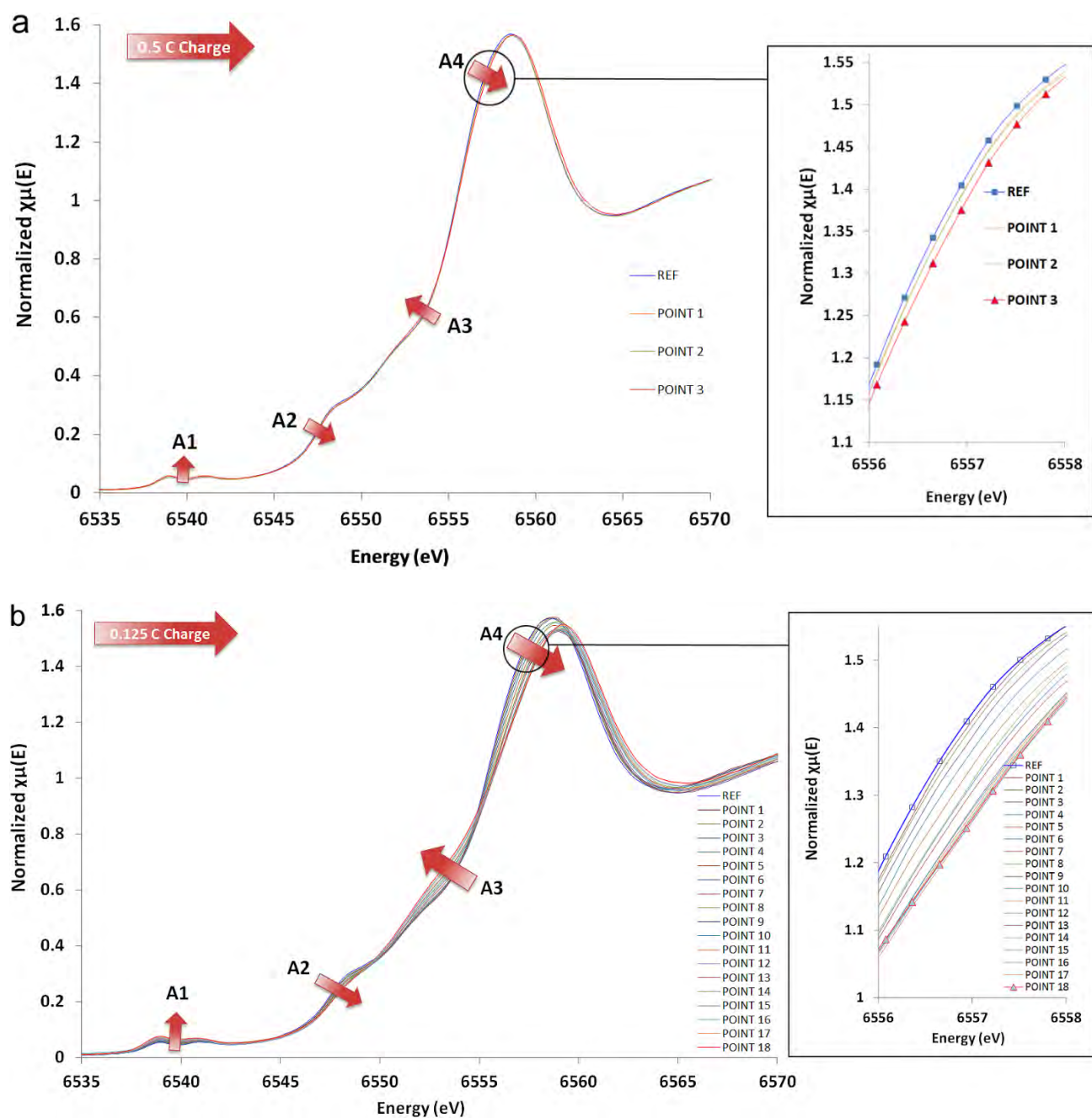


Fig. 3. Normalised XANES spectra (k^3 -weighted) at Mn K-edge of $\text{Li}(\text{Li}_{0.2}\text{Mn}_{0.54}\text{Ni}_{0.13}\text{Co}_{0.13})\text{O}_2$ during the initial charge (a) Distinctive absorptions and the trend of the spectra shift in the fast charge (0.5 C) cell (G1). (b) Distinctive absorptions and the trend of the spectra shift in the slow charge (0.125 C) cell (G2). POINT signifies the collection point of XAS spectra and it is numbered as 1, 2 ...18, which corresponds to the charge points in the galvanostatic profile. REF indicates the measurement point of the coin cell without any current.

The voltage profiles of the lithium-ion cells are presented in **Fig. 2d,e**. For the fast charge cell (G1), a total of four points of XAS could be taken during the initial charge, whilst for the slow charge cell (G2), 19 data points were collected. For each data set, the XAS collection began at the ‘REF’ point at which no current was applied. **Fig. 3** compares the XANES results

obtained at the Mn K-edge from cell G1 (charge rate of 0.5 C) and cell G2 (charge rate of 0.125 C). Four significant features (A1- A4) are indicated in the absorption at the Mn K-edge, with the red arrows representing the direction of spectral changes during charging. Absorption feature A2 in **Fig. 3a** can be associated with the electric dipole transition from 1s to 4p accompanied by a shakedown process attributed to the ligand-to-metal charge transfer (LMCT), while feature A4 corresponds to the electric dipole transition from 1s to 4p without the shakedown process. The final states of feature 2 and 4 correspond to $1s^1c3d^{n+1}L4p^1$ and $1s^1c3d^nL4p^1$, respectively, where c is a 1s core hole and L is an oxygen 2p ligand (Mn^{4+} : $n=3$). The decrease of the peak intensity in feature A4 that accompanies charging indicates the suppression of the tetragonal distortion in the MnO_6 octahedron, possibly via the Ni substitution. The spectral shift for Mn amounts to only 0.4 eV in the fast charge cell G1 (**Fig. 3a**), while it equals 1.3 eV for the slow charge cell G2 (**Fig. 3b**). This possibly implies an oxidation change in the slow charge cell. It is generally known that the oxidation state of Mn is +4 in the pristine material and remains unchanged during charge. However, a number of studies [32,46] have found that the Mn in the pristine material may exist in a mixed oxidation state between low-spin Mn^{3+} and Mn^{4+} . Double pre-edge peaks were found between 6538 and 6543 eV at the Mn K-edge. The pre-edge peaks rose upon charge, and the trend of energy shifts was similar at both charge rates, as indicated by the red arrows in **Fig. 4a,b**. However, at the slow charge rate increase in the peak intensity was four times higher than at the fast charge rate. These peaks are assigned to 1s-3d_{t2g} (lower energy) and 1s-3d_{eg} (higher energy) transitions, which is formally dipole-electric forbidden in a centrosymmetric system. These peaks appear from a weak quadrupole transition or/and 3d-4p orbital hybridization from the loss of centrosymmetric environment by the distortion of the octahedral 3a site in the $R\bar{3}m$ space group. Hence, information about the atomic geometry can be deduced from the intensity of the peaks. Higher intensity signifies the octahedral structure that is distorted away from the centrosymmetric environment. The slow charge cell (G2) revealed higher structural distortion

during Li^+ deintercalation. It should be also noted that the energy difference between $1s-3d_{t_{2g}}$ and $1s-3d_{e_g}$ transitions decreases during the initial charge, and this can be well observed in the slow charge cell as presented in **Fig. 4b**.

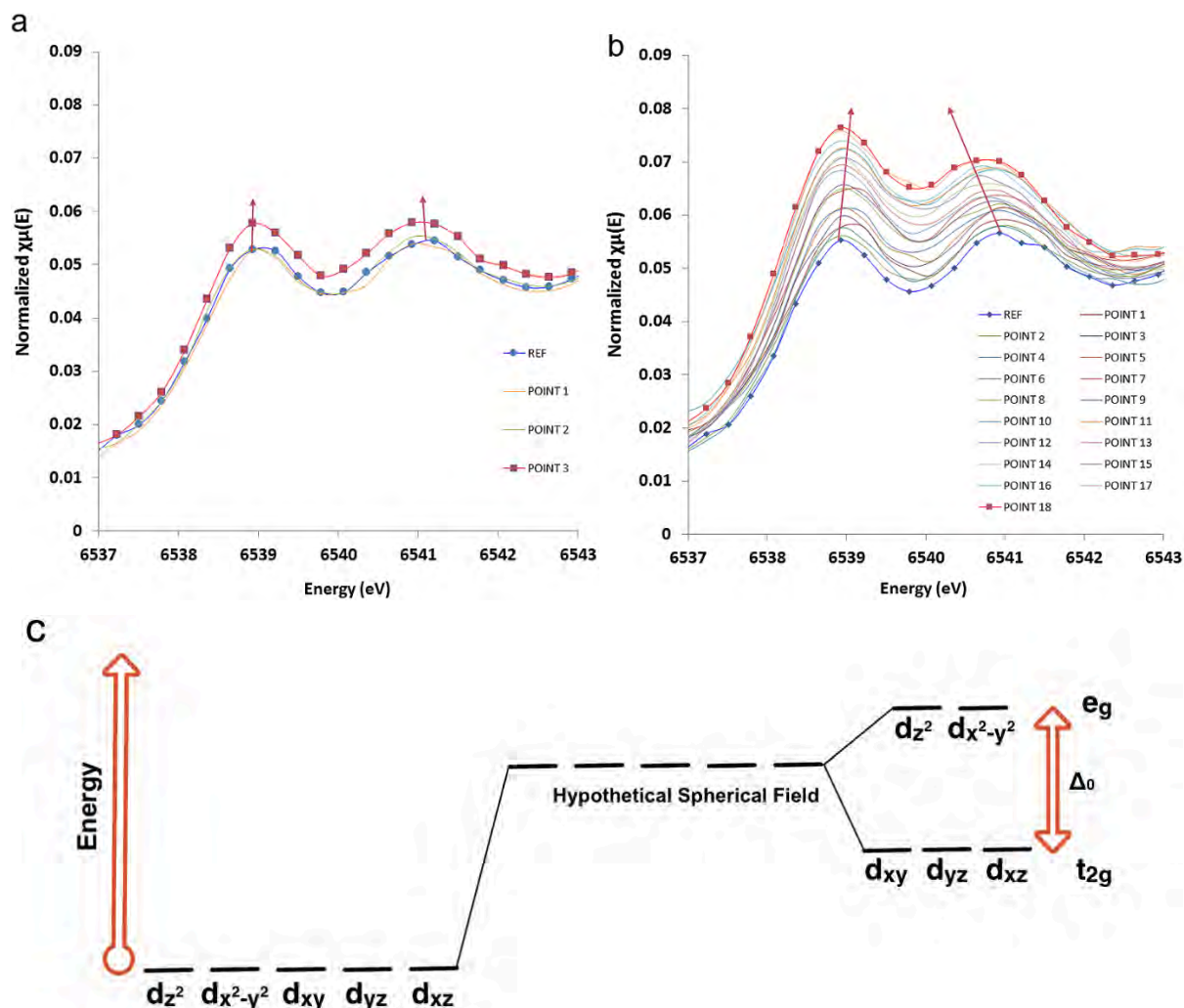


Fig. 4. Normalised XANES spectra (k^3 -weighted) at Mn K pre-edge of $\text{Li}(\text{Li}_{0.2}\text{Mn}_{0.54}\text{Ni}_{0.13}\text{Co}_{0.13})\text{O}_2$ during the initial charge at (a) fast charge (0.5 C) and (b) slow charge (0.125 C) cells. (c) Illustration of the crystal field splitting diagram of d-orbitals in Mn octahedral environment. Δ_0 denotes crystal field splitting energy.

The observation can be explained by the crystal field theory for the octahedral geometry in transition metals (**Fig. 4c**). A free transition metal ion remains degenerate with the same energy level of five $3d$ orbitals (d_z^2 , $d_{x^2-y^2}$, d_{xy} , d_{xz} , and d_{yz}). If the Mn atom is encircled by a spherically symmetrical field of negative charges, the five $3d$ orbitals remain still degenerate with an increased energy level. However, when Mn forms an octahedral complex with the ligand atoms (O^{2-}), the degeneracy of the d orbitals is removed and this leads to the energy

splitting of the two d orbital groups. The energy difference between the two sets of d orbitals is the crystal field splitting energy which is denoted by Δ_o . At the 'REF' state where no current was applied, the energy difference between t_{2g} and e_g was approximately 2 eV on both charge rates. The crystal field splitting energy Δ_o declined from 2 eV at REF to 1.42 eV at POINT 18.

3.2. *In Operando XANES at Co K-edge*

XANES spectra collected at the Co K-edge during the initial charge are shown in **Fig. 5**. The direction of the spectra shift in the G2 cell was similar to that of G1 cell, as they moved towards higher energy during the charge. However, there was a significant difference in the magnitude of the spectral shift between the fast and slow charge cells, as can be seen in **Fig. 5a,b**. The spectral shift of the Co K-edge in G1 the cell was 0.61 eV, whereas a larger spectral shift (1.41 eV) was observed in the G2 cell. The spectral shifts toward higher energy indicate the increase in the oxidation state, e.g from Co^{3+} to Co^{4+} . The oxidation change of Co ions stems from the compensation process for the Li^+ deintercalation of the active material. There was a similarity in the oxidation state trend between Co and Mn upon initial charge. This similarity could be attributed to the similar local environment since those transition metals can occupy same position in the crystal structure of $\text{R}\bar{3}\text{m}$.

Fig. 6a,b shows the XANES spectra collected at the Co K pre-edge for G1 and G2 cells, respectively. Lower intensity peaks were recorded at around 7708.8 eV at the Co K-edge in XANES. In contrast to the Mn K pre-edge, the appearance of the pre-edge peaks at Co K-edge could be attributed to the 1s to 3d transition. The intensity of those peaks in the fast charge cell (G1) reveals continuous rise in the normalized intensity during the charge, as illustrated in **Fig. 6a**. However, no significant trend was observed in the slow charge cell (G2). This finding implies a difference in the reaction impact on the host structure as a

function of the charge rate, due to the different origin of Li^+ deintercalation. This is discussed in more detail in the discussion section.

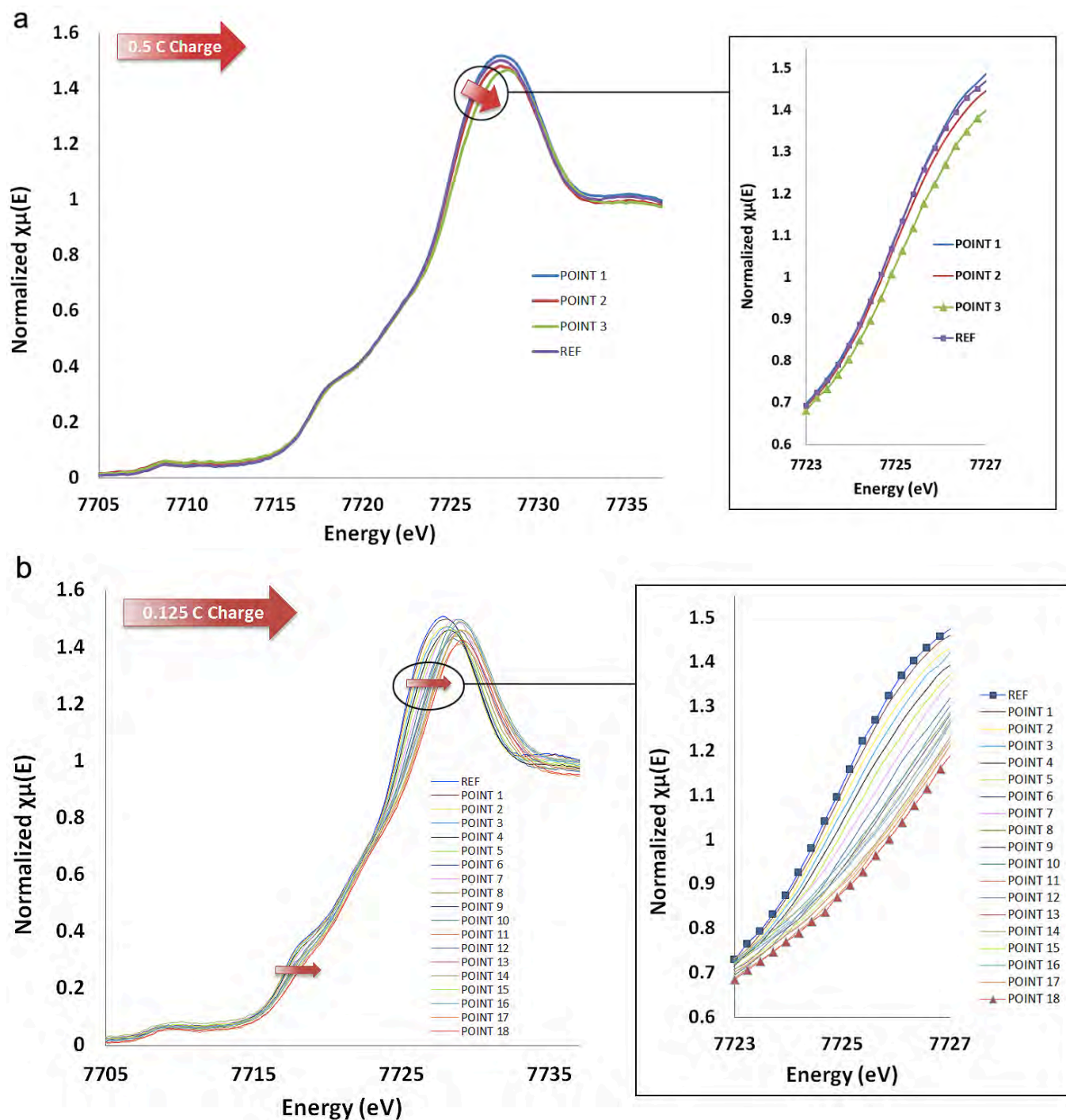


Fig. 5. Normalised XANES spectra (k^3 -weighted) at Co K-edge of $\text{Li}(\text{Li}_{0.2}\text{Mn}_{0.54}\text{Ni}_{0.13}\text{Co}_{0.13})\text{O}_2$ during the initial charge of (a) fast charge (0.5 C) and (b) slow charge (0.125 C) cells.

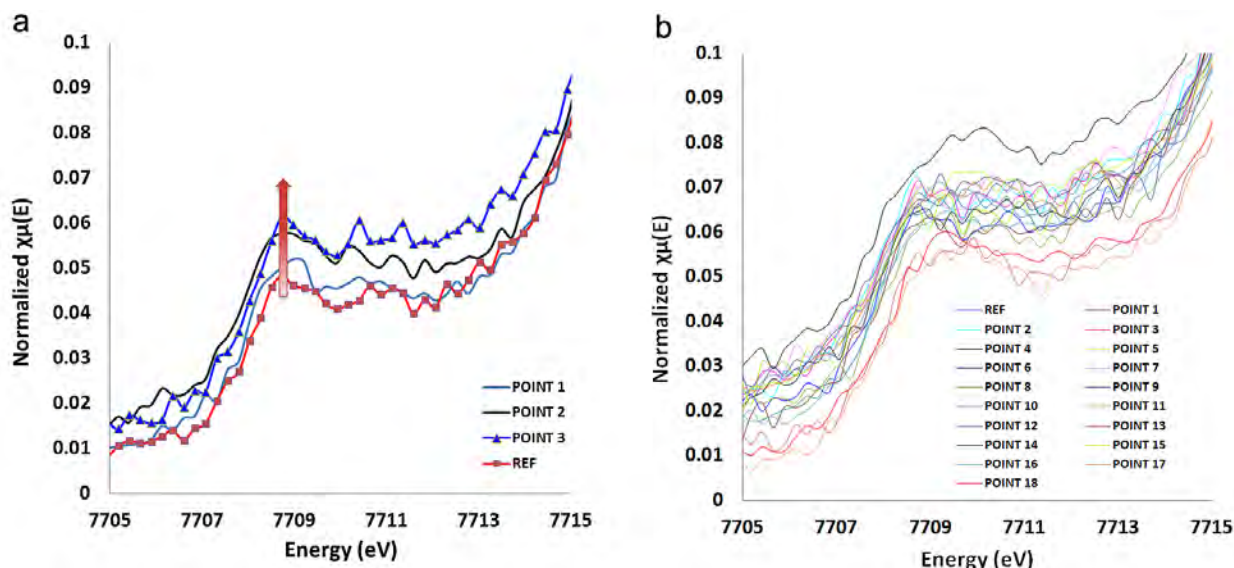


Fig. 6. Normalised XANES spectra (k^3 -weighted) at Co K pre-edge of $\text{Li}(\text{Li}_{0.2}\text{Mn}_{0.54}\text{Ni}_{0.13}\text{Co}_{0.13})\text{O}_2$ during the initial charge of (a) fast charge (0.5 C) and (b) slow charge (0.125 C) cells.

3.3. In Operando XANES at Ni K-edge

Fig. 7a,b presents the results obtained from the normalised XANES spectra at Ni K edge during the initial charge of G1 and G2 cells, respectively. Ni XANES spectra shift towards higher energy upon charge. This pattern can be compared with the trends in the Mn XANES spectra. There were no pre-edge peaks noted in the Ni XANES in the range 8330-8335 eV stemming from the $1s \rightarrow 3d$ transition. It is therefore likely that the atomic environment of Ni in the cathode material is highly symmetrical. A parallel energy shift can be observed in Ni XANES indicating a different local environment compared with that of Mn. The K-edge energy shift of Ni towards the higher energy is attributed to nickel oxidation. Up to the fully charged state, the energy shift of the G1 cell (**Fig. 7a**) from the reference point to the fully charged point was approximately 1.07 eV, while the energy shift of the G2 cell (**Fig. 7b**) was approximately 2.6 eV. The relatively smaller shift of the G1 cell implies smaller oxidation changes in the cathode. The oxidation state of nickel in the fully discharged state is reported to be +2, or a mixed state between +2 and +3, while the oxidation state in the fully charged state is described as a mixed state between +3 and +4 [21,42].

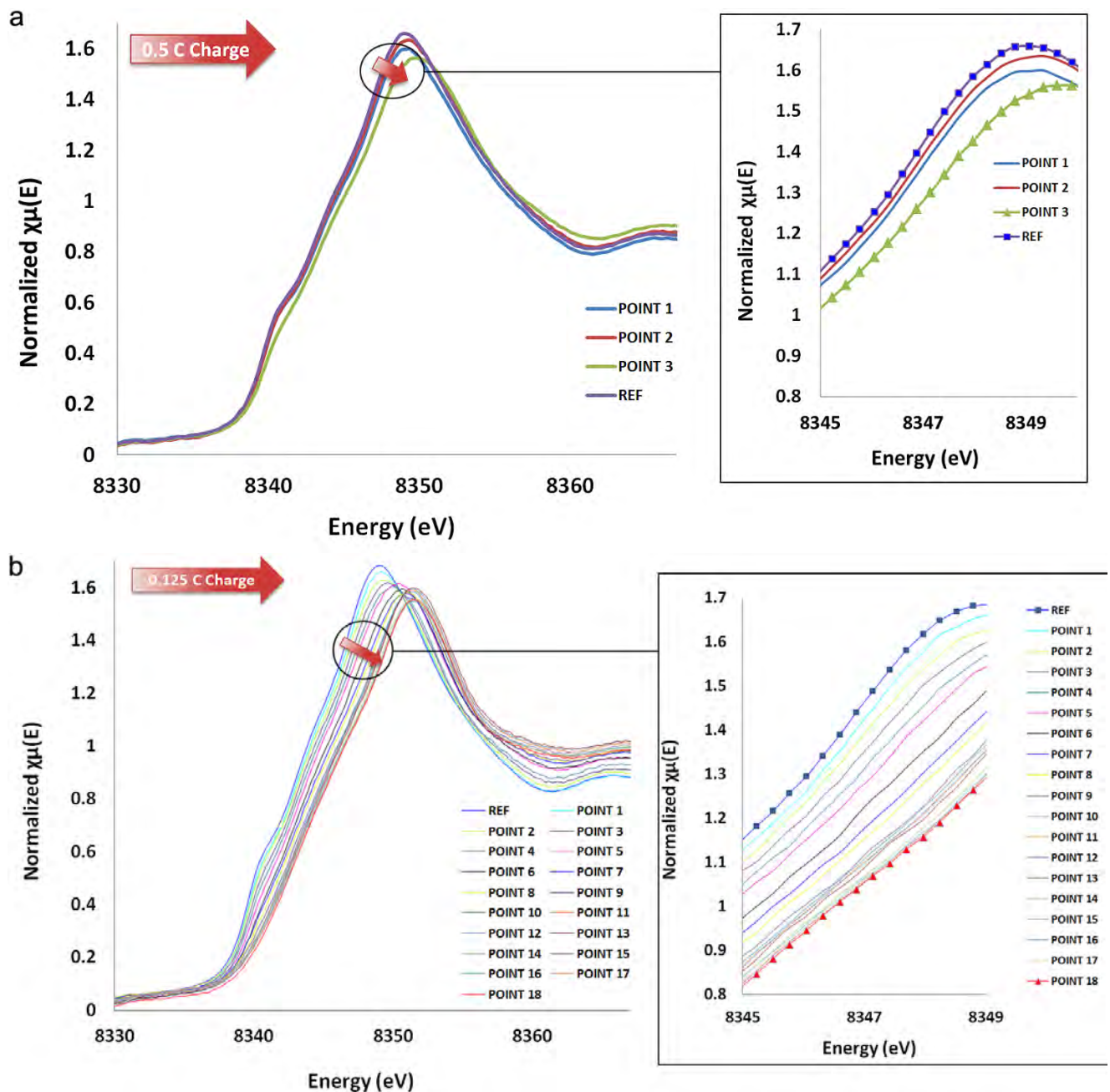


Fig. 7. Normalised XANES spectra (k³-weighted) at Ni K-edge of Li(Li_{0.2}Mn_{0.54}Ni_{0.13}Co_{0.13})O₂ during the initial charge of (a) fast charge (0.5 C) and (b) slow charge (0.125 C) cells.

Ni revealed the largest energy shifts of XANES spectra at K-edge compared with Mn and Co. This result may be explained by the multiple steps of the Ni oxidation change [21], such as $\text{Ni}^{2+} \rightarrow \text{Ni}^{3+} \rightarrow \text{Ni}^{4+}$, whereas Co reveals a single step oxidation change. More than double the energy shift was found in the slow charge cell. It is likely that fewer Ni^{3+} Jahn-Teller ions appeared in the fast charge during the Li^+ deintercalation, leading to a minimum impact on the host structure.

3.4. In Operando EXAFS at Mn K-edge

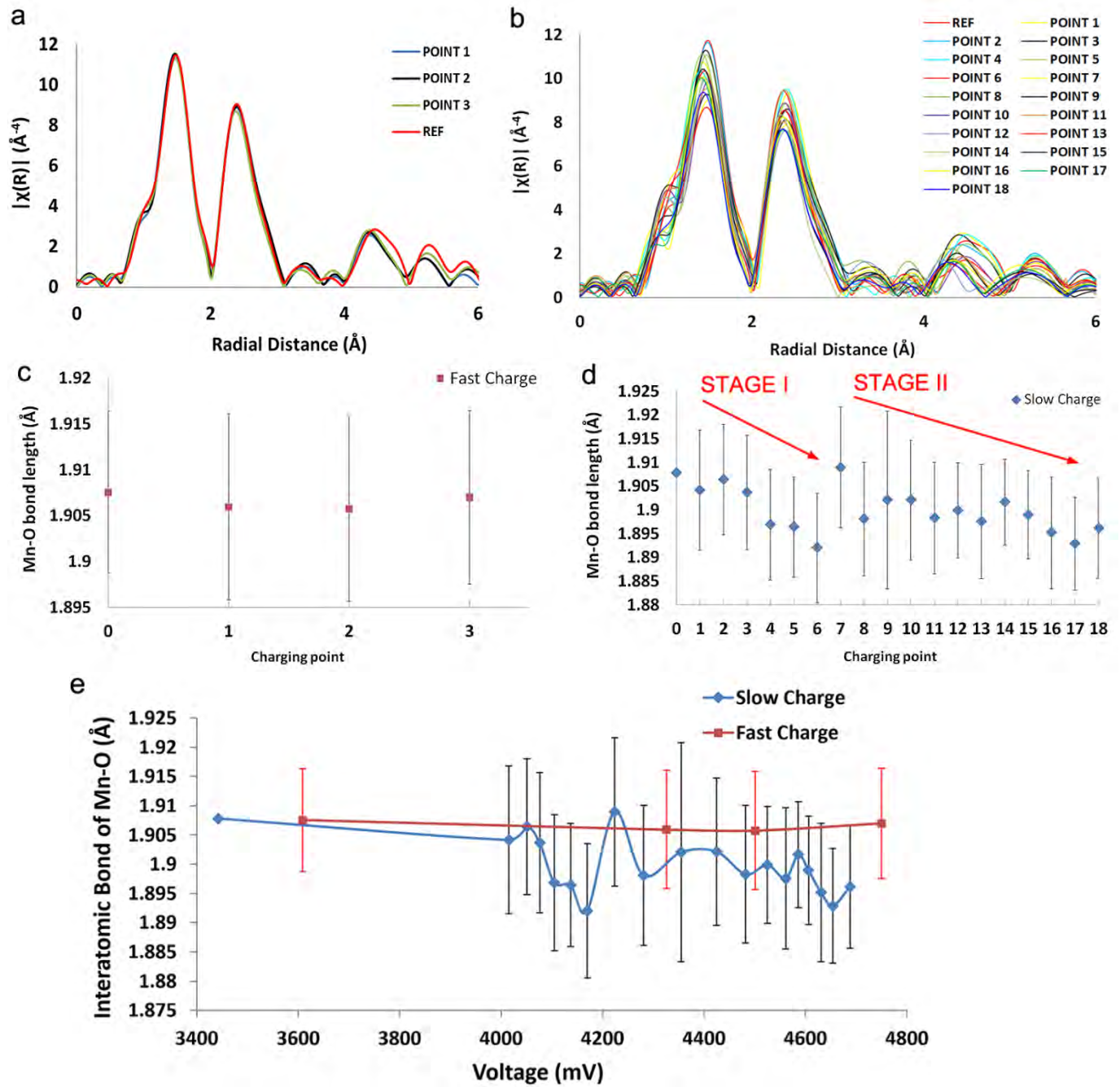


Fig. 8. Fourier transform magnitudes (k^3 -weighted) at Mn K-edge of the graphene-coated $\text{Li}(\text{Li}_{0.2}\text{Mn}_{0.54}\text{Ni}_{0.13}\text{Co}_{0.13})\text{O}_2$ during charge of (a) fast charged (0.5 C) G1 and (b) slow charged (0.125 C) G2 cells. Evaluation of the atomic bond-lengths of (c) G1 1st shell (Mn-O) and (d) G2 1st shell (Mn-O). (e) Comparison of Mn-O changes vs voltage during charge. POINT signifies the collection point of XAS spectra and it is numbered as 1, 2 ...18, which corresponds to the charge points in the galvanostatic profile. REF (point 0) indicates the measurement point of the coin cell without any current.

Fig. 8 provides the R-space (real space) result obtained from the Fourier transform of Mn EXAFS of the graphene-coated $\text{Li}(\text{Li}_{0.2}\text{Mn}_{0.54}\text{Ni}_{0.13}\text{Co}_{0.13})\text{O}_2$ cathode during initial charge.

The R-space chart reveals that there has been a decrease in the level of the intensity from the

first peak (Mn-O) during the initial charge, and this trend is clearly reflected in the slow charge cell (**Fig. 8b**). The intensity of the first peak at ~ 1.53 Å at slow charge rate dropped by 27%, whereas it only dropped by 1.1% at fast charge rate. The fast charge cell is less likely than the slow charge cell to deviate from the EXAFS pattern in R-space at the reference point (REF) during charge, as presented in **Fig. 8a**. It can thus be suggested that the slow charge, a deep charge process, leads to higher impact on the host structure of the cathode. From **Fig. 8** it is apparent that the slow charge rate led to larger bond length changes of Mn-O than the fast charge rate. The maximum difference of the bond length was 0.016 Å in the slow charge, and 0.001 Å in the fast charge cells. The distinctive impact from the charge rate dynamic is highlighted by this comparison. Bond length changes of Mn-O/Mn-TM (TM: Mn, Co, and Ni) were evaluated during the initial charge. The coordination number was constrained to be 6 for the Mn fitting, while major EXAFS parameters such as EXAFS Debye-Waller factor, mean square disorder (σ^2), and R-factors were refined by the calculation. The evaluation of the Mn-O bond lengths from both charge rates can be compared in **Fig. 8c,d**. It is interesting to note the possible presence of two stages in the local environment change at the slow charge rate can be seen **Fig. 8c**. The second stage begins from approximately the charge point 7 (G2 cell) where the voltage corresponds to ~ 4.224 V in the galvanostatic profile. The two-stage reaction was clearly identified in the slow charge cell whereas it was not apparent in the fast charge cell, perhaps due to the limited number of measurement points available.

3.5. In Operando EXAFS at Co K-edge

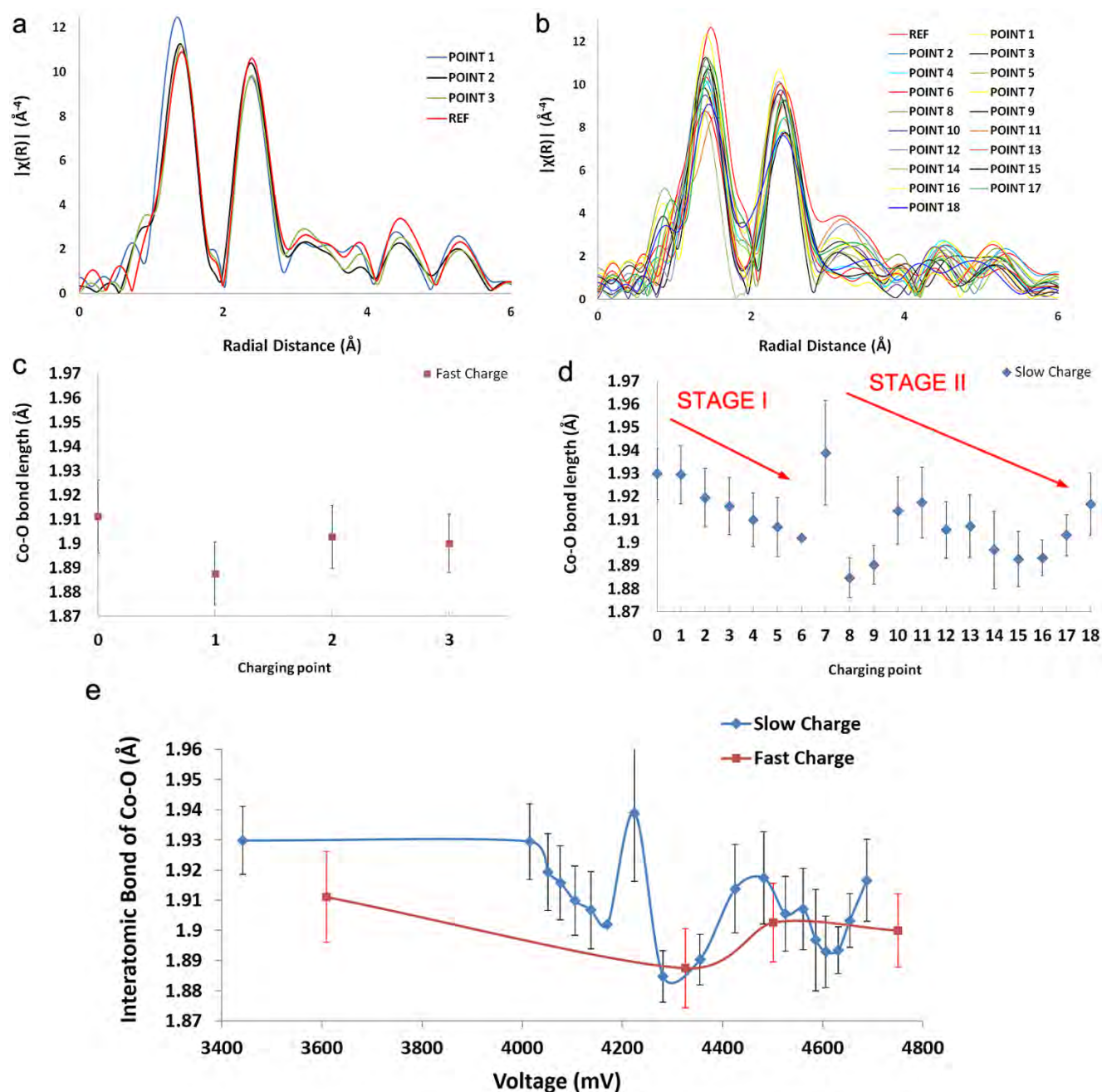


Fig. 9. Fourier transform magnitudes (k^3 -weighted) at Co K-edge of the graphene-coated $\text{Li}(\text{Li}_{0.2}\text{Mn}_{0.54}\text{Ni}_{0.13}\text{Co}_{0.13})\text{O}_2$ during charge of (a) fast charged G1 (0.5 C) and (b) slow charged G2 (0.125 C) cells. Evaluation of the atomic bond-lengths of (c) G1 1st shell (Co-O) and (d) G2 1st shell (Co-O). (e) Comparison of Co-O changes vs voltage during charge. POINT signifies the collection point of XAS spectra and it is numbered as 1, 2 ...18, which corresponds to the charge points in the galvanostatic profile. REF (point 0) indicates the measurement point of the coin cell without any current.

The results obtained from the Fourier transforms of Co EXAFS in the R-space during initial charge are presented in **Fig. 9**. The coordination number was constrained to be 6 for the fitting of the Co-O/Co-TM pairs. Other EXAFS parameters for Co were refined by the fitting

calculation. The impacts from different charge rates on the host structure are similar to those for Mn. Slower charge rate exhibits larger deviations from the reference EXAFS signal during the charge (**Fig. 9a,b**). This aspect is well reflected in **Fig. 9e**, where the Co-O bond length changes are reported at the slow charge rate. The two-stage reaction in the Co local environment at the slow charge rate was also clearly identified, as shown in **Fig. 9c**. The second stage is likely to start from charge point 7 (G2 cell), where the voltage corresponds to ~4.2-4.3 V in the galvanostatic profile, i.e. in the range identical to that of Mn. It is obvious from the Co EXAFS analysis that the slow charge revealed distinctive bond length changes with the maximum difference of 0.054 Å, while the fast charge presented relatively small changes with the maximum difference of 0.024 Å upon the initial charge.

3.6. *In Operando EXAFS at Ni K-edge*

Fig. 10a,b shows the Fourier transforms of Ni EXAFS in the R-space during initial charge. The result indicates some significant inconsistency of the EXAFS patterns in the R-space between the spectra collected during charge, as compared with Mn and Co EXAFS. This finding suggests that the local atomic environment of Ni varies more remarkably during Li⁺ deintercalation. The complicated local environment changes of Ni can be explained by several factors, such as cation mixing between Li⁺ and Ni²⁺, Jahn-Teller distortion from the Ni³⁺ ion, and the two-step oxidation (Ni²⁺ → Ni³⁺ → Ni⁴⁺) of Ni. Especially, the differentiation of the Ni-O bonds (**Fig. 10c,d**) that begins approximately from 4.224 V is attributed to the Jahn-Teller distortion effect from Ni³⁺. By this observation, the two stages can be also identified in the local environment changes of Ni during the initial charge as illustrated in **Fig. 10c**, and the range of those stages appears to be consistent with those for Mn and Co. Both cells are likely to reveal Ni distortion from approximately 4.224 V, but the bond-length difference between the Ni-O and Ni-O (short) was more considerable in the slow

charge rate (G2 cell). The bond-length difference was estimated to be 0.0343 Å at 4.224 V, and increased up to 0.1595 Å at the slow charge rate.

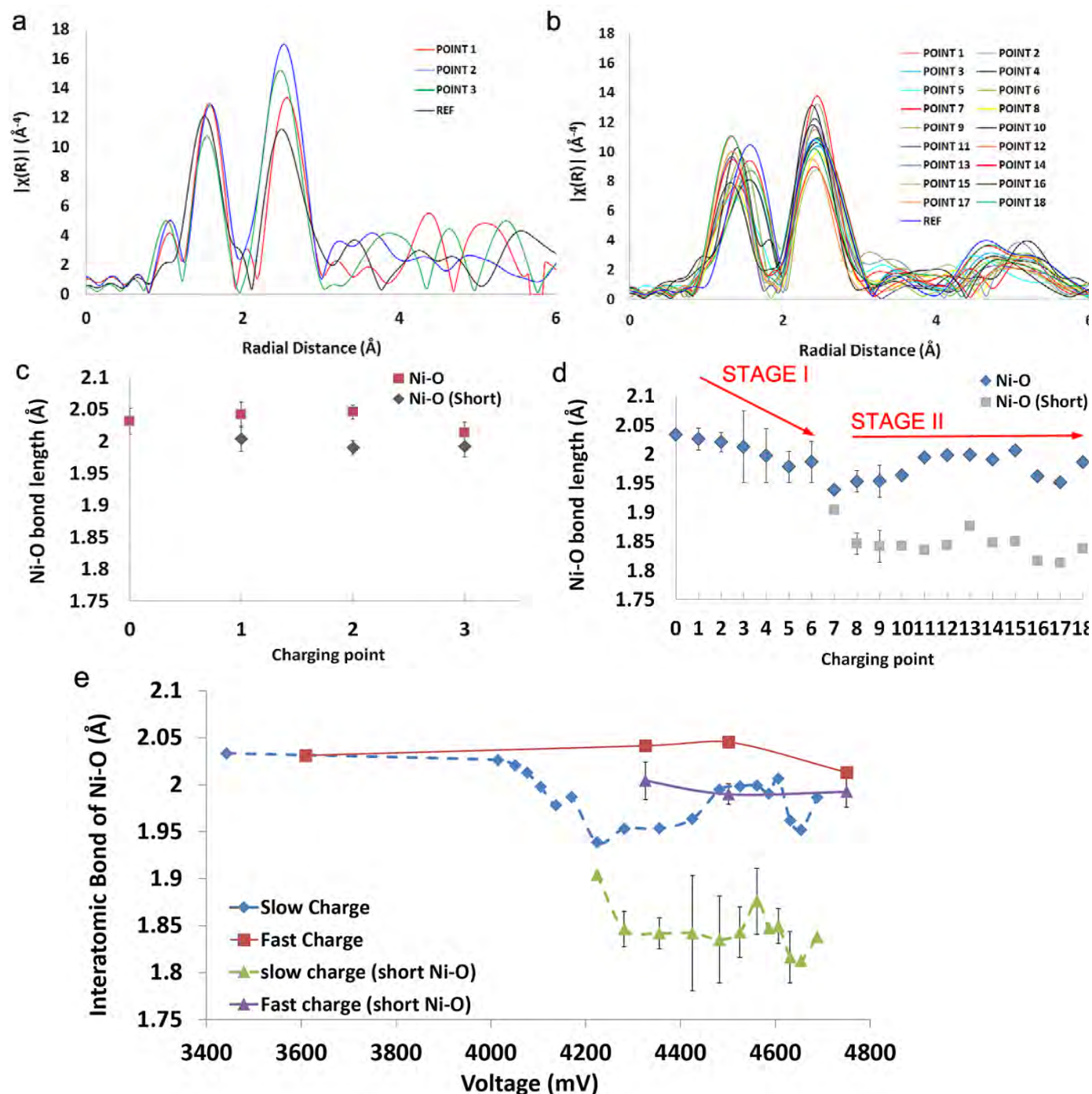


Fig. 10. Fourier transform magnitudes (k^3 -weighted) at Ni K-edge of the graphene-coated $\text{Li}(\text{Li}_{0.2}\text{Mn}_{0.54}\text{Ni}_{0.13}\text{Co}_{0.13})\text{O}_2$ during charge of (a) fast charged G1 and (b) slow charged G2 cells. Evaluation of the atomic bond-lengths of (c) G1 1st shell (Ni-O) and (d) G2 1st shell (Ni-O). (e) Comparison of Ni-O changes vs voltage during charge. POINT signifies the collection point of XAS spectra and it is numbered as 1, 2 ...18, which corresponds to the charge points in the galvanostatic profile. REF (point 0) indicates the measurement point of the coin cell without any current.

Similarly, the difference was calculated to be 0.0373 Å at 4.224 V at the fast charge rate, but only reached up to 0.0556 Å, i.e. three times smaller than the slow charge rate. Therefore, the slow charge cell tends to undergo larger structural changes in comparison with the fast charge cell. From **Fig. 10e** it is apparent that the fast charge rate revealed more significant changes in the Ni local environment than the slow charge rate. EXAFS fitting for Ni was performed with the coordination number of 6 and EXAFS parameters were refined during the fitting computation. From charge point 7 in the G2 cell, the coordination number of 4 and 2 were used for the fitting of the long Ni-O and short Ni-O bonds, respectively. The coordination numbers for Ni-O varied according to the state of charge in both cells.

4. Discussion

The mechanism of Li^+ diffusion in the layered oxide cathode can be described by the hopping process from one MO_6 octahedral site to another MO_6 octahedral site via a tetrahedral site, where the transition metal repels the Li^+ ion [28], as illustrated in **Fig. 1**. Generally, Li^+ extraction from the host material appears either simultaneously or sequentially both from the Li-layer and the transition metal layer [21,23]. However, Li^+ ions tend to be extracted from the transition-metal layer more deeply under the slow charging condition, which exerts considerable influence on the underlying structure. The distinct influences can be deduced and compared on the basis of EXAFS interpretation. The maximum bond length difference for Mn-O was measured to be 0.001 Å in the fast charge cell, and 0.016 Å in the slow charge cell. The maximum difference in the Co-O bond length was calculated to be 0.024 Å for the fast charge cell, and 0.054 Å for the slow charge cell. The Mn-O bond length at the slow charge rate decreased until charge POINT 6. Immediately after this point, a sudden rise in the bond length was observed at charge POINT 7 corresponding to ~4.224 V. This observation can be explained by the crystal lattice change in the trigonal system ($R\bar{3}m$) during

the initial charge. Previous studies [3,10,22–24,27] have revealed the increase of the c-lattice parameter and a decrease in the a-lattice parameter during charge by *in situ* XRD. Especially, the expansion of the c-lattice is likely to be explained by the electrostatic repulsion between the oxygen ions after the extraction of the Li^+ from the intermediate lithium layer between them. The observed trend, including the sudden rise in the bond-length, has not been reported in the case of fast charge rate. The maximum difference in the Co-O bond length was calculated to be 0.024 Å for the fast charge cell, and 0.054 Å for the slow charge cell. Similarly, a sudden rise in the Co-O bond length was noted at charge POINT 7, with no similar trend observed in the case of fast charge rate. The maximum difference in the Ni-O bond length at slow charge rate was 0.220 Å, whereas it was only 0.055 Å at fast charge rate. It appears that the Ni atom local environment undergoes relatively higher structural changes with increased charge rate. The process interpretation becomes more complicated when the Jahn-Teller distortion from Ni^{3+} is considered in the EXAFS analysis. We were able to examine the Ni-O bond splitting resulting from the Jahn-Teller effect at the same charge point (POINT 7 / 4.224 V) where a sudden rise in the bond length was note in the Mn-O and Co-O results. The bond-length difference between the long Ni-O and short Ni-O bonds reached maximum at 4.482 V as 0.159 Å for the slow charge and 4.501 V as 0.055 Å for the fast charge cells (**Fig. 10e**).

Changes in the oxidation/electronic states of the transition metals were also compared. While the XAS investigation did not confirm the exact oxidation numbers of each transition metal, it did allow us to quantify the energy shifts of the XANES spectra during the initial charge. The spectral shifts of Mn, Co, and Ni K-edge were 0.4 eV, 0.61 eV, and 1.07 eV in the fast charge cell (G1), respectively. Larger spectral shifts could be observed in the slow charge cell (G2), namely, 1.3 eV, 1.41 eV, and 2.6 eV for Mn, Co, and Ni K-edge, respectively. To better identify the difference, the XANES spectra shifts were also compared at same chemical potentials. The largest spectral shift at the Ni K-edge is likely to be

attributed to the two-step oxidation change ($\text{Ni}^{2+} \rightarrow \text{Ni}^{3+} \rightarrow \text{Ni}^{4+}$). It can be suggested that fewer Ni^{3+} ions appeared in the fast charge cell during Li^+ deintercalation, so that the structure underwent less distortion from the Jahn-Teller ion (Ni^{3+}). The trend of the parallel energy shift in Ni XANES suggests a different local environment compared to that of Mn and Co. This study also identified the crystal field splitting at the Mn K pre-edge from the double peaks (**Fig. 4**). The crystal field splitting energy (Δ_o) decreases as lithium ions deintercalate from the active material. This signifies the increased number of unpaired electrons of Mn during deintercalation. There was a clear trend of the energy splitting at the slow charge rate. It appears that the slow rate can give rise to the large numbers of electrons provided from Mn for Li^+ diffusion.

Taken together, the *in operando* XAS results suggest that the nature of the structural changes in the mixed transition metal cathode is likely to be different depending on the charge rate. Whereas the change at the slow charge rate seems to be irreversible, the local environment change in the cathode at fast charge rate appears to be reversible, because the length of the inter-atomic bonds tends to return to its initial condition during further charge in the fast charge cell. In Ni EXAFS, two-stage reaction with Ni-O bond splitting was examined. The differentiation of the Ni-O bond length in the fast charge cell was small, and the bond-length difference was tiny at the last charge point (4.750 V), implying the return to the single type Ni-O bond. However, the splitting impact from Ni^{3+} at 4.224 V persisted over a large range of charge points, until the last charge POINT 18 in the slow charge cell. It may be the case therefore that the changes observed at the slow charge rate points at the phase transition from the layered oxide to spinel phase during electrochemical cycling. This is widely regarded as an irreversible phase change [22,44]. However, the structural change at the faster charge rate does not appear to lead to irreversible phase transition from layered oxide to spinel structure, due to the smaller range of the plateau in terms of voltage (stage 2) in the galvanostatic profile of the fast charge cell (**Fig. 2d**). These combined observations suggest

that there may exist an optimum range of charge rates determined based on the consideration of phase differentiation for particular cathode materials, aimed to maximize the performance and ensure enhanced stability of the battery.

5. Conclusion

This study has demonstrated, for the first time, the distinctive difference in the structural impact on the TM local environments of the different charge rates (0.125 C vs 0.5 C) by *in operando* XAS investigation on the graphene-coated $\text{Li}(\text{Li}_{0.2}\text{Mn}_{0.54}\text{Ni}_{0.13}\text{Co}_{0.13})\text{O}_2$ battery cathodes. The key finding from the current study is the identification of the separation of the two local-atomic environments at 4.224 V stemming from the activation of the Li_2MnO_3 composite in the high voltage range for each transition metal (Mn, Co, and Ni). However, the two-stage reaction in the local environment was clearly observed only in the slow charge cell (G2) in the EXAFS analyses. It is likely that the Li^+ deintercalation mechanism changes depending on the charge rate. The empirical findings from synchrotron XAS analyses assist in the understanding of the charge rate sensitivity (0.5 C vs 0.125 C) during Li^+ deintercalation. The novel design of the *in operando* coin cells was crucial for enabling this research. This study delivers new insight into combined tailoring of the optimal charge rates for a particular structure of the high capacity cathode in order to minimize irreversible phase transitions that lead to irreversible capacity loss.

Acknowledgements

The authors acknowledge the support for the use of the synchrotron source at the B18 Core EXAFS beamline at Diamond Light Source (DLS, UK) under the rapid access scheme with proposal number SP 4004.

References

- [1] J.B. Goodenough, Y. Kim, Challenges for Rechargeable Li Batteries †, *Chem. Mater.* 22 (2010) 587–603. doi:10.1021/cm901452z.
- [2] M. Armand, J.-M. Tarascon, Building better batteries., *Nature.* 451 (2008) 652–7. doi:10.1038/451652a.
- [3] M.M. Thackeray, S.-H. Kang, C.S. Johnson, J.T. Vaughey, S. a. Hackney, Comments on the structural complexity of lithium-rich $\text{Li}_{1+x}\text{M}_{1-x}\text{O}_2$ electrodes (M=Mn, Ni, Co) for lithium batteries, *Electrochem. Commun.* 8 (2006) 1531–1538. doi:10.1016/j.elecom.2006.06.030.
- [4] T.A. Arunkumar, Y. Wu, A. Manthiram, Factors Influencing the Irreversible Oxygen Loss and Reversible Capacity in Layered $\text{Li}[\text{Li}_{1/3}\text{Mn}_{2/3}]\text{O}_2\text{-Li}[\text{M}]\text{O}_2$ (M= $\text{Mn}_{0.5-y}\text{Ni}_{0.5-y}\text{Co}_{2y}$ and $\text{Ni}_{1-y}\text{Co}_y$) Solid Solutions., *Chem. Mater.* 19 (2007) 3067–3073. doi:10.1021/cm070389q.
- [5] F. Amalraj, D. Kovacheva, M. Talianker, L. Zeiri, J. Grinblat, N. Leifer, et al., Synthesis of Integrated Cathode Materials $x\text{Li}_2\text{MnO}_3(1-x)\text{LiMn}_{1/3}\text{Ni}_{1/3}\text{Co}_{1/3}\text{O}_2$ ($x = 0.3, 0.5, 0.7$) and Studies of Their Electrochemical Behavior, *J. Electrochem. Soc.* 157 (2010) A1121–A1130. doi:10.1149/1.3463782.
- [6] Z. Lu, D.D. MacNeil, J.R. Dahn, Layered Cathode Materials $\text{Li}[\text{Ni}_x\text{Li}_{(1/3-2x/3)}\text{Mn}_{(2/3-x/3)}]\text{O}_2$ for Lithium-Ion Batteries, *Electrochem. Solid-State Lett.* 4 (2001) A191. doi:10.1149/1.1407994.
- [7] H. Deng, I. Belharouak, R.E. Cook, H. Wu, Y.-K. Sun, K. Amine, Nanostructured Lithium Nickel Manganese Oxides for Lithium-Ion Batteries, *J. Electrochem. Soc.* 157 (2010) A447. doi:10.1149/1.3308598.
- [8] Y. Wu, A. Vadivel Murugan, A. Manthiram, Surface Modification of High Capacity Layered $\text{Li}[\text{Li}_{0.2}\text{Mn}_{0.54}\text{Co}_{0.13}\text{Ni}_{0.13}]\text{O}_2$ Cathodes by AlPO_4 , *J. Electrochem. Soc.* 155 (2008) A635. doi:10.1149/1.2948350.
- [9] K. Ben-Kamel, N. Amdouni, A. Mauger, C.M. Julien, Study of the local structure of $\text{LiNi}_{0.33+\delta}\text{Mn}_{0.33+\delta}\text{Co}_{0.33-2\delta}\text{O}_2$ ($0.025 \leq \delta \leq 0.075$) oxides, *J. Alloys Compd.* 528 (2012) 91–98. doi:10.1016/j.jallcom.2012.03.018.
- [10] J.-M. Kim, H.-T. Chung, The first cycle characteristics of $\text{Li}[\text{Ni}_{1/3}\text{Co}_{1/3}\text{Mn}_{1/3}]\text{O}_2$ charged up to 4.7 V, *Electrochim. Acta.* 49 (2004) 937–944. doi:10.1016/j.electacta.2003.10.005.
- [11] S.J. Jin, C.H. Song, K.S. Park, A.M. Stephan, K.S. Nahm, Y.S. Lee, et al., The effect of compositional change of transition metals on the electrochemical behavior of layered LiMO_2 (M= $\text{Li}_w\text{Ni}_x\text{Co}_y\text{Mn}_z$) solid solutions, *J. Power Sources.* 158 (2006) 620–626. doi:10.1016/j.jpowsour.2005.10.007.
- [12] N. Yabuuchi, T. Ohzuku, Novel lithium insertion material of $\text{LiCo}_{1/3}\text{Ni}_{1/3}\text{Mn}_{1/3}\text{O}_2$ for advanced lithium-ion batteries, *J. Power Sources.* 119-121 (2003) 171–174. doi:10.1016/S0378-7753(03)00173-3.
- [13] T.J. Boyle, D. Ingersoll, M.A. Rodriguez, C.J. Tafoya, D.H. Doughty, An Alternative Lithium Cathode Material: Synthesis, Characterization, and Electrochemical Analysis of $\text{Li}_8(\text{Ni}_5\text{Co}_2\text{Mn})\text{O}_{16}$, *J. Electrochem. Soc.* 146 (1999) 1683–1686. <http://jes.ecsdl.org/content/146/5/1683.short>.

- [14] B. Song, M.O. Lai, L. Lu, Influence of Ru substitution on Li-rich $0.55\text{Li}_2\text{MnO}_3 \cdot 0.45\text{LiNi}_{1/3}\text{Co}_{1/3}\text{Mn}_{1/3}\text{O}_2$ cathode for Li-ion batteries, *Electrochim. Acta*. 80 (2012) 187–195. doi:10.1016/j.electacta.2012.06.118.
- [15] S.-H. Kang, Y.K. Sun, K. Amine, Electrochemical and Ex Situ X-Ray Study of $\text{Li}(\text{Li}_{0.2}\text{Ni}_{0.2}\text{Mn}_{0.6})\text{O}_2$ Cathode Material for Li Secondary Batteries, *Electrochem. Solid-State Lett.* 6 (2003) A183. doi:10.1149/1.1594411.
- [16] R. Armstrong, M. Holzapfel, P. Novák, C.S. Johnson, S.H. Kang, M.M. Thackeray, et al., Demonstrating oxygen loss and associated structural reorganization in the lithium battery cathode $\text{Li}[\text{Ni}_{0.2}\text{Li}_{0.2}\text{Mn}_{0.6}]\text{O}_2$, *J. Am. Chem. Soc.* 128 (2006) 8694–8698. doi:10.1021/ja062027+.
- [17] Z. Lu, L.Y. Beaulieu, R. a. Donabarger, C.L. Thomas, J.R. Dahn, Synthesis, Structure, and Electrochemical Behavior of $\text{Li}[\text{Ni}_x\text{Li}_{1/3-2x/3}\text{Mn}_{2/3-x/3}]\text{O}_2$, *J. Electrochem. Soc.* 149 (2002) A778. doi:10.1149/1.1471541.
- [18] G.Y. Kim, S.B. Yi, Y.J. Park, H.G. Kim, Electrochemical behaviors of $\text{Li}[\text{Li}_{(1-x)/3}\text{Mn}_{(2-x)/3}\text{Ni}_{x/3}\text{Co}_{x/3}]\text{O}_2$ cathode series ($0 < x < 1$) synthesized by sucrose combustion process for high capacity lithium ion batteries, *Mater. Res. Bull.* 43 (2008) 3543–3552. doi:10.1016/j.materresbull.2008.01.011.
- [19] C.S. Johnson, J.-S. Kim, C. Lefief, N. Li, J.T. Vaughey, M.M. Thackeray, The significance of the Li_2MnO_3 component in “composite” $x\text{Li}_2\text{MnO}_3 \cdot (1-x)\text{LiMn}_{0.5}\text{Ni}_{0.5}\text{O}_2$ electrodes, *Electrochem. Commun.* 6 (2004) 1085–1091. doi:10.1016/j.elecom.2004.08.002.
- [20] A.R. Armstrong, A.D. Robertson, P.G. Bruce, Overcharging manganese oxides : Extracting lithium beyond Mn^{4+} , 146 (2005) 275–280. doi:10.1016/j.jpowsour.2005.03.104.
- [21] N. Yabuuchi, K. Yoshii, S.-T. Myung, I. Nakai, S. Komaba, Detailed Studies of a High-Capacity Electrode Material for Rechargeable Batteries, $\text{Li}_2\text{MnO}_3\text{--LiCo}_{1/3}\text{Ni}_{1/3}\text{Mn}_{1/3}\text{O}_2$, *J. Am. Chem. Soc.* 133 (2011) 4404–4419. doi:10.1021/ja108588y.
- [22] D. Mohanty, S. Kalnaus, R. a. Meisner, K.J. Rhodes, J. Li, E.A. Payzant, et al., Structural transformation of a lithium-rich $\text{Li}_{1.2}\text{Co}_{0.1}\text{Mn}_{0.55}\text{Ni}_{0.15}\text{O}_2$ cathode during high voltage cycling resolved by in situ X-ray diffraction, *J. Power Sources*. 229 (2013) 239–248. doi:10.1016/j.jpowsour.2012.11.144.
- [23] H.H. Li, N. Yabuuchi, Y.S. Meng, S. Kumar, J. Breger, C.P. Grey, et al., Changes in the Cation Ordering of Layered O3 $\text{Li}_x\text{Ni}_{0.5}\text{Mn}_{0.5}\text{O}_2$ during Electrochemical Cycling to High Voltages: An Electron Diffraction Study, *Chem. Mater.* 19 (2007) 2551–2565. doi:10.1021/cm070139+.
- [24] Z. Lu, J.R. Dahn, Understanding the Anomalous Capacity of $\text{Li}/\text{Li}[\text{Ni}_x\text{Li}_{(1/3-2x/3)}]\text{Mn}_{(2/3-x/3)}\text{O}_2$ Cells Using In Situ X-Ray Diffraction and Electrochemical Studies, *J. Electrochem. Soc.* 149 (2002) A815. doi:10.1149/1.1480014.
- [25] M.M. Thackeray, S.-H. Kang, C.S. Johnson, J.T. Vaughey, R. Benedek, S. a. Hackney, Li_2MnO_3 -stabilized LiMO_2 ($\text{M} = \text{Mn}, \text{Ni}, \text{Co}$) electrodes for lithium-ion batteries, *J. Mater. Chem.* 17 (2007) 3112. doi:10.1039/b702425h.
- [26] Y.S. Meng, G. Ceder, C.P. Grey, W.-S. Yoon, M. Jiang, J. Bréger, et al., Cation Ordering in Layered O3 $\text{Li}[\text{Ni}_x\text{Li}_{1/3-2x/3}\text{Mn}_{2/3-x/3}]\text{O}_2$ ($0 \leq x \leq 1$), *Chem. Mater.* 17 (2005) 2386–2394. doi:10.1021/cm047779m.

- [27] N. Tran, L. Croguennec, M. Ménétrier, F. Weill, P. Biensan, C. Jordy, et al., Mechanisms Associated with the “Plateau” Observed at High Voltage for the Overlithiated $\text{Li}_{1.12}(\text{Ni}_{0.425}\text{Mn}_{0.425}\text{Co}_{0.15})_{0.88}\text{O}_2$ System, *Chem. Mater.* 20 (2008) 4815–4825. doi:10.1021/cm070435m.
- [28] K. Kang, G. Ceder, Factors that affect Li mobility in layered lithium transition metal oxides, *Phys. Rev. B.* 74 (2006). doi:10.1103/PhysRevB.74.094105.
- [29] K. Kang, Y.S. Meng, J. Bréger, C.P. Grey, Gerbrand Ceder, Electrodes with High Power and High Capacity for Rechargeable Lithium Batteries, *Science* (80-.). 311 (2006) 977–980. doi:10.2307/3843557.
- [30] A. Rougier, P. Gravereau, C. Delmas, Optimization of the Composition of the $\text{Li}_{1-z}\text{Ni}_{1+z}\text{O}_2$ Electrode Materials: Structural, Magnetic, and Electrochemical Studies, *J. Electrochem. Soc.* 143 (1996) 1168–1175. doi:10.1149/1.1836614.
- [31] E. Zhecheva, R. Stoyanova, R. Alcántara, P. Lavela, J.-L. Tirado, Cation order/disorder in lithium transition-metal oxides as insertion electrodes for lithium-ion batteries, *Pure Appl. Chem.* 74 (2002). doi:10.1351/pac200274101885.
- [32] L. Simonin, J.-F. Colin, V. Ranieri, E. Canévet, J.-F. Martin, C. Bourbon, et al., In situ investigations of a Li-rich Mn–Ni layered oxide for Li-ion batteries, *J. Mater. Chem.* 22 (2012) 11316. doi:10.1039/c2jm31205k.
- [33] M. Jiang, B. Key, Y.S. Meng, C.P. Grey, Electrochemical and Structural Study of the Layered, “Li-Excess” Lithium-Ion Battery Electrode Material $\text{Li}[\text{Li}_{1/9}\text{Ni}_{1/3}\text{Mn}_{5/9}]\text{O}_2$, *Chem. Mater.* 21 (2009) 2733–2745. doi:10.1021/cm900279u.
- [34] J.R. Croy, K.G. Gallagher, M. Balasubramanian, Z. Chen, Y. Ren, D. Kim, et al., Examining Hysteresis in Composite $x\text{Li}_2\text{MnO}_3 \cdot (1-x)\text{LiMO}_2$ Cathode Structures, *J. Phys. Chem. C.* 117 (2013) 6525–6536. doi:10.1021/jp312658q.
- [35] R.E. Johnsen, P. Norby, Capillary-based micro-battery cell for in situ X-ray powder diffraction studies of working batteries: a study of the initial intercalation and deintercalation of lithium into graphite, *J. Appl. Crystallogr.* 46 (2013) 1537–1543. doi:10.1107/S0021889813022796.
- [36] G. Singh, W.C. West, J. Soler, R.S. Katiyar, In situ Raman spectroscopy of layered solid solution $\text{Li}_2\text{MnO}_3\text{--LiMO}_2$ ($\text{M} = \text{Ni}, \text{Mn}, \text{Co}$), *J. Power Sources.* 218 (2012) 34–38. doi:10.1016/j.jpowsour.2012.06.083.
- [37] S.K. Martha, J. Nanda, G.M. Veith, N.J. Dudney, Surface studies of high voltage lithium rich composition: $\text{Li}_{1.2}\text{Mn}_{0.525}\text{Ni}_{0.175}\text{Co}_{0.1}\text{O}_2$, *J. Power Sources.* 216 (2012) 179–186. doi:10.1016/j.jpowsour.2012.05.049.
- [38] R. Baddour-Hadjean, J.-P. Pereira-Ramos, Raman Microspectrometry Applied to the Study of Electrode Materials for Lithium Batteries, *Chem. Rev.* 110 (2010) 1278–1319. doi:10.1021/cr800344k.
- [39] P. Lanz, C. Villevieille, P. Novák, Electrochemical activation of Li_2MnO_3 at elevated temperature investigated by in situ Raman microscopy, *Electrochim. Acta.* 109 (2013) 426–432. doi:10.1016/j.electacta.2013.07.130.
- [40] A.R. Armstrong, N. Dupre, A.J. Paterson, C.P. Grey, P.G. Bruce, Combined Neutron Diffraction, NMR, and Electrochemical Investigation of the Layered-to-Spinel Transformation in LiMnO_2 , *Chem. Mater.* 16 (2004) 3106–3118. doi:10.1021/cm034964b.

- [41] A. Ito, Y. Sato, T. Sanada, M. Hatano, H. Horie, Y. Ohsawa, In situ X-ray absorption spectroscopic study of Li-rich layered cathode material $\text{Li}[\text{Ni}_{0.17}\text{Li}_{0.2}\text{Co}_{0.07}\text{Mn}_{0.56}]\text{O}_2$, *J. Power Sources*. 196 (2011) 6828–6834. doi:10.1016/j.jpowsour.2010.09.105.
- [42] J.R. Croy, M. Balasubramanian, D. Kim, S.-H. Kang, M.M. Thackeray, Designing High-Capacity, Lithium-Ion Cathodes Using X-ray Absorption Spectroscopy, *Chem. Mater.* 23 (2011) 5415–5424. doi:10.1021/cm2026703.
- [43] M. Oishi, T. Fujimoto, Y. Takanashi, Y. Orikasa, A. Kawamura, T. Ina, et al., Charge compensation mechanisms in $\text{Li}_{1.16}\text{Ni}_{0.15}\text{Co}_{0.19}\text{Mn}_{0.50}\text{O}_2$ positive electrode material for Li-ion batteries analyzed by a combination of hard and soft X-ray absorption near edge structure, *J. Power Sources*. 222 (2013) 45–51. doi:10.1016/j.jpowsour.2012.08.023.
- [44] B. Song, M.O. Lai, Z. Liu, H. Liu, L. Lu, Graphene-based surface modification on layered Li-rich cathode for high-performance Li-ion batteries, *J. Mater. Chem. A*. 1 (2013) 9954–9965. doi:10.1039/C3TA11580A.
- [45] B. Ravel, M. Newville, ATHENA, ARTEMIS, HEPHAESTUS: Data analysis for X-ray absorption spectroscopy using IFEFFIT, *J. Synchrotron Radiat.* 12 (2005) 537–541. doi:10.1107/S0909049505012719.
- [46] J.K. Ngala, N.A. Chernova, L. Matienzo, P.Y. Zavalij, M. Stanley, The Syntheses and Characterization of Layered LiNi, in: Cambridge Univ Press, 2003: pp. 4–9. <http://journals.cambridge.org/production/action/cjoGetFulltext?fulltextid=8072766>.